



Tropical cyclone intensity classification from infrared images of clouds over Bay of Bengal and Arabian Sea using machine learning classifiers

Chinmoy Kar¹ · Sreeparna Banerjee²

Received: 15 October 2020 / Accepted: 22 March 2021
© Saudi Society for Geosciences 2021

Abstract

Tropical cyclones are natural phenomena occurring in coastal tropical regions that cause damage to life and property. Hence, a study of their evolution is necessary to prevent loss of life and property. In this paper, we present a cloud intensity classification technique for tropical cyclones based on feature extraction and pattern recognition, over the Bay of Bengal and Arabian Sea basins (latitudes 5° N–22° N and longitudes 52° E–100° E). Images of ten cyclones (2013 to 2018) are collected from the TC archive of Marine Meteorology Division of the US Naval Research Laboratory. A novel set of features is used for this purpose using some geometric properties of the cyclone structure. These features are fed to five machine learning classifiers: Naïve Bayes, Support Vector Machine, Logistic Model Tree, Random Tree and Random Forest. The Random Forest classifier used here for classification task outperforms other classifiers with an accuracy of 86.66%. It is also observed that the root mean square error of the Random Forest classifier maximum sustained wind speed is 9.84 knots. Results indicate that the proposed feature extraction technique and machine learning classifiers are feasible for the tropical cyclone intensity classification from infrared images.

Keywords Tropical cyclone · Tropical cyclone intensity · Center of gravity · Random Forest · Image processing

Introduction

Cyclones in the Bay of Bengal and Arabian Sea (or typhoons as they are known in the Pacific Ocean or hurricanes in the Atlantic Ocean) constitute devastating natural phenomena. Hence, a thorough understanding of their origin, structure, evolution, and behavior near landfall is necessary for forecasting and prevention of loss (Dube et al. 1997, 2009; Frank and Ritchie 1999; Takahashi 2011; Arora and Jha 2016). Therefore, a study of different aspects of cyclone development

is necessary for forecasting and mitigation of damage. Several research groups have focused on these different aspects, namely, cyclogenesis, track analysis, and cyclone evolution studies, from cyclone cloud intensity data. In this study, we analyze cyclone cloud intensity patterns near landfall, from infrared (IR) images taken by geostationary satellites (Pao and Yeh 2008; Drönner et al. 2018). These images are obtained from the best track data, i.e., cloud intensities observed at the cyclone latitude and longitude at half hourly intervals (<https://www.nrlmry.navy.mil/tcdat>).

Traditional approaches to cyclone evolution analyses are pattern matching and wind field analysis (Jin et al. 2017; Jaiswal and Kishtawal 2013; Yip et al. 2006). The Saffir–Simpson scale (Saffir 1973; Simpson 1974; National Oceanic and Atmospheric Administration 2021) is a scale used to characterize the evolutionary sequence of a cyclone based on wind field analysis (Cardone and Cox 2009; Ritchie et al. 2012, 2014; Kotal and Bhattacharya 2020). Present-day wind speed analysis methods typically use Numerical Weather Prediction (NWP) (Numerical Weather Prediction Division IMD 2021; NOAA 2021; Pu and Kalnay 2019) combined with pattern analysis to study the evolution of cyclones (RSMC New Delhi 2019) (TPC-21 2018), starting from cyclogenesis.

Responsible Editor: Biswajeet Pradhan

✉ Chinmoy Kar
chinmoy.k@smit.smu.edu.in

Sreeparna Banerjee
sreeparnab@hotmail.com

¹ Department of Computer Science and Engineering, Sikkim Manipal Institute of Technology, Sikkim Manipal University, Gangtok, Sikkim, India

² Department of Natural Science, Maulana Abul Kalam Azad University of Technology, Kolkata, India

The classifications of tropical cyclone (TC) images based on the cloud pattern are curved bands, shear, central dense overcast pattern, and eye. Curved bands are spiral structures which are seen when the cyclone is in developing stage. Shear patterns are more curved around the center of a TC. The central dense overcast (CDO) cloud pattern is with a circular structure without a clear eye. Eye structure of a TC is a well-defined center established in developed TC.

Most popular pattern recognition-based classifications of TCs were based on cloud intensity patterns using the Dvorak technique and its variants (Dvorak 1975, 1984; Velden et al. 2006), which is applied manually to TC images using a rule-based algorithm. In the Dvorak technique, which is a rule-based technique, the intensity value depends on the extent of the cyclone cloud patterns and their banding, as well as the CDO. T numbers were assigned to the different stages of evolution in the original Dvorak technique. The T number can be correlated with wind speed analysis (Dvorak 1975; Fetanat et al. 2013). These techniques are manual and hence subjective in nature as they depend on skills of the user. The objective Dvorak technique (ODT) developed by Velden et al. in 2006 was the first attempt to automate the Dvorak technique. However, this technique could only analyze strong cyclones and depended on the user to locate the storm center. The advanced Dvorak technique (ADT) (Olander et al. 2002; Olander and Velden 2007) is incorporated with several improvements like better storm center detection and regression-based image analysis to compute the intensity present on the eye or CDO, and modification of original Dvorak intensity rules. More recent versions of the Dvorak technique ADT version 8 and ADT version 9 (Olander and Velden 2019) can also perform pattern analysis on microwave images. Other pattern recognition approaches based on the Dvorak technique include eye-based methods (Griffin et al. 1992; Wood 1994; Yeh et al. 2012) and approaches which involve the extraction of contours of the dominant cyclones and cyclone structures (Lee and Lin 2001; Zhang et al. 2010; Pineros et al. 2008; Dutta and Banerjee 2013).

Modern-day cyclone cloud intensity analysis uses artificial intelligence (AI)-based approaches. In particular, machine learning (ML) algorithms are used for classification after the feature selection process. K-nearest neighbor (KNN) (Bankert and Tag 2002) using 15 features and artificial neural network (ANN) (Kulkarni et al. 2010) using 36 features have been tried with a good measure of success. Some other approaches in this category have been reported in the literature (Sakuragi et al. 2014; Roy 2016; Kar et al. 2019a; Chen et al. 2018). ML algorithms have also been used to study cyclogenesis (Zhang et al. 2019) and intensity from wind speed analysis. In particular, the Random Forest algorithm has been studied for cyclogenesis (Kim et al. 2019).

Recently, the convolution neural network (CNN) is being explored for cyclone cloud intensity analysis (Liu et al. 2016;

Pradhan et al. 2018; Yu et al. 2020; Combinido et al. 2018) from IR images. CNN algorithms have been used for intensity analysis from wind speed data (Lee et al. 2020; Chen et al. 2018; Yu et al. 2019; Chen et al. 2019) using multispectral (MSI) images as well as in cyclogenesis (Matsuoka et al. 2018). Typically, three layers are used in this architecture. The convolution layers extract local features from the input images to form feature maps, which are used in the pooling layers to permit spatial invariance by decreasing the image resolution. Most correlated features of a particular class are deciphered from fully connected. Thus, a huge number of features are extracted automatically from the input images. These features result in a huge dimensionality of the feature vector. In the Chen et al. (2019) paper, this dimensionality is reduced using principal component analysis (PCA), while Yu et al. (2019) used Tucker decomposition, a tensor networking technique. The process is data driven, so unsupervised algorithms cannot be applied. On the other hand, a large number of training sets are required for supervised algorithms and this is not readily available, so existing datasets must be replicated in order to build a large training set and this does not provide much new information. Chen et al. (2019) used a semi-supervised algorithm with small number of training sets. The CNN is used twice to perform iterative training update using a hybrid similarity measurement. This is cumbersome. Lee et al. (2020), Combinido et al. (2018), and Pradhan et al. (2018) use IR images to classify the different stages of cyclone cloud evolution. However, in all these techniques, the images are fed into the input layer which acts like a black box and extracts a huge number of features automatically. The user has no control over the features used or their suitability for the classification process. Furthermore, the huge number of features poses a curse of dimensionality problem which has to be reduced by PCA or tensor networks. Also, the non-availability of training sets which is compensated by replicating the existing datasets does not add to the information content. These disadvantages result in a limitation in the use of CNN as a viable cyclone intensity classification technique.

The eye of a cyclone is essentially a region of calm weather and is roughly located at the center of the tropical cyclone. The eyewall surrounding the eye is a ring of thunderstorms and the most dangerous part of the cyclone. The air in the eyewall moves faster than in other areas, thus drawing moisture from the ocean causing thunderstorms and extending rain-bands. The degree of spiraling or banding determines the intensity of the cyclone. This spiral helix-like appearance of the TC cloud leads to the possibility of analysis of the cloud pattern and its temporal evolution using geometry-based features. The utility of such features has also been studied in our earlier works (Kar and Banerjee 2016, 2018; Kar et al. 2019a, b).

In this work, we present a new feature extraction and pattern recognition-based technique using the following machine learning classifiers: Naïve Bayes, Support Vector Machine,

Random Tree, Logistic Model Tree, and Random Forest. Low-level geometric and statistical features are used and their suitability is also studied and ranks are apportioned to these features, accordingly. The novelty of this method lies in the use of simple geometric features, which are size, translation, and rotation invariant features. Thus, these features can be used universally for all different cyclones occurring at different times. A small dataset is required for the usage of this algorithm. The location of the eye of a cyclone is unessential as the algorithm is translation invariant. Moreover, such a study has not been conducted before for the Bay of Bengal (BoB) and Arabian Sea (AS) basins, to the best of our knowledge.

The paper is organized as follows. The data sources used are mentioned in the “[Data source](#)” section, followed by a description of our methodology in the “[Methodology](#)” section. A brief description about classifiers is mentioned in the “[Classifiers](#)” section. Results and discussion are given in the “[Results](#)” and “[Discussion](#)” sections with conclusions stated in the “[Conclusion](#)” section.

Data source

Geostationary meteorological satellite images

Images of Meteosat-8 and Meteosat-7 satellite products are used here. Meteosat-8 is stationed over the Indian Ocean at longitude of 41.5° E and 36,000 km above the equator (Observing Systems Capability Analysis and Review Tool 2021). Meteosat-8 replaced Meteosat-7 on February 2017. Meteosat-7 sends images every 30 min, whereas Meteosat-8 collects images every 15 min. Meteosat-8 has 11 channels/bands (Dröner et al. 2018). IR channels 7–11 are IR8.7 to IR13.4. Images of these IR channels are processed further for feature extraction due to their availability in the website of the US Naval Research Laboratory (Table 1).

TC images are collected from the US Naval Research Laboratory. Infrared images of TC over the Bay of Bengal (BOB) and Arabian Sea (ARB) from 2013 to 2017 are selected for the study. Satellite image specification and other information are shown in Table 2.

The InfraRed (IR) satellite images are obtained from the Bay of Bengal and Arabian Sea. Different geographical regions have different cyclone behavior patterns and are studied

Table 2 Details of image archive

Website	https://www.nrlmry.navy.mil/tcdat
Owner	US Naval Research Laboratory
TC covered year	2018 to 2013
Satellite	Meteosat-8 and Meteosat-7
Channels used	Infrared (IR)
Basins	Indian Ocean

by the Regional Specialized Meteorological Centre (RSMC) and Indian Meteorological Department (IMD). These cyclone intensity patterns are studied by considering six classes. These classes are analogous to the six classes of Chen et al. (2019) and Yu et al. (2019) for typhoons in the Pacific, whereas Lee et al. (2020) used seven classes following the Saffir–Simpson scale. The proposed classification model based on the TC intensity scale is given in Table 3.

Details TC images

The total number of images of each class is 100. To make the dataset balance, VSCS and ESCS TCs are selected from 2013 to 2018. In Table 4, the intensity-wise numbers of images of TCs from 2018 to 2013 (last 6 years) are mentioned.

NA not available (image of TC is not available)

Methodology

The entire work is divided into two parts. First, feature extraction techniques were applied on input images, followed by the classification of images by the abovementioned six classes using the extracted features. The feature extraction methodologies are used to extract features from the rotation-size-translation invariant images which are explained in the “[Image pre-processing](#)” section. Finally, the extracted features are used in ML-based classifiers. The flowchart of the proposed work is shown in Fig. 1.

Image pre-processing

- The original images of size 1024×1024 pixels are resized to 256×256 pixels.

Table 1 Specification of Meteosat satellites

Satellite name	Wavelength range (μm) of IR channel	Spatial resolution (km)	Temporal resolution (min.)
Meteosat-8	8.7–13.4 μm	4	15
Meteosat-7	10.5–12.5 μm	5	30

Table 3 TC intensity scale (TPC-21 2018)

Intensity scale	Sustained winds speed
Extremely severe cyclonic storm (ESCS)	90–119 knots 166–220 km/h
Very severe cyclonic storm (VSCS)	64–89 knots 118–165 km/h
Severe cyclonic storm (SCS)	48–63 knots 89–117 km/h
Cyclonic storm (CS)	34–47 knots 63–88 km/h
Deep depression (DD)	28–33 knots 51–62 km/h
Depression (D)	17–27 knots 31–50 km/h

- The resized image is further used to find the center of gravity (CoG) (Barnes and Manic 2010). The CoG of a TC image is calculated based on the formula given below:

$$m_{cog} = \left(\sum_{m=1}^i \sum_{n=1}^j m * c_{mn} \right) / \left(\sum_{m=1}^i \sum_{n=1}^j c_{mn} \right) \quad (1)$$

$$n_{cog} = \left(\sum_{m=1}^i \sum_{n=1}^j n * c_{ij} \right) / \left(\sum_{m=1}^i \sum_{n=1}^j c_{mn} \right) \quad (2)$$

where the total number of horizontal pixels is i , and total number of vertical pixels is j of image C . C_{mn} is the m th and n th element of an image (C) and m_{cog} and n_{cog} are used to denote the pixel coordinate of the entire image.

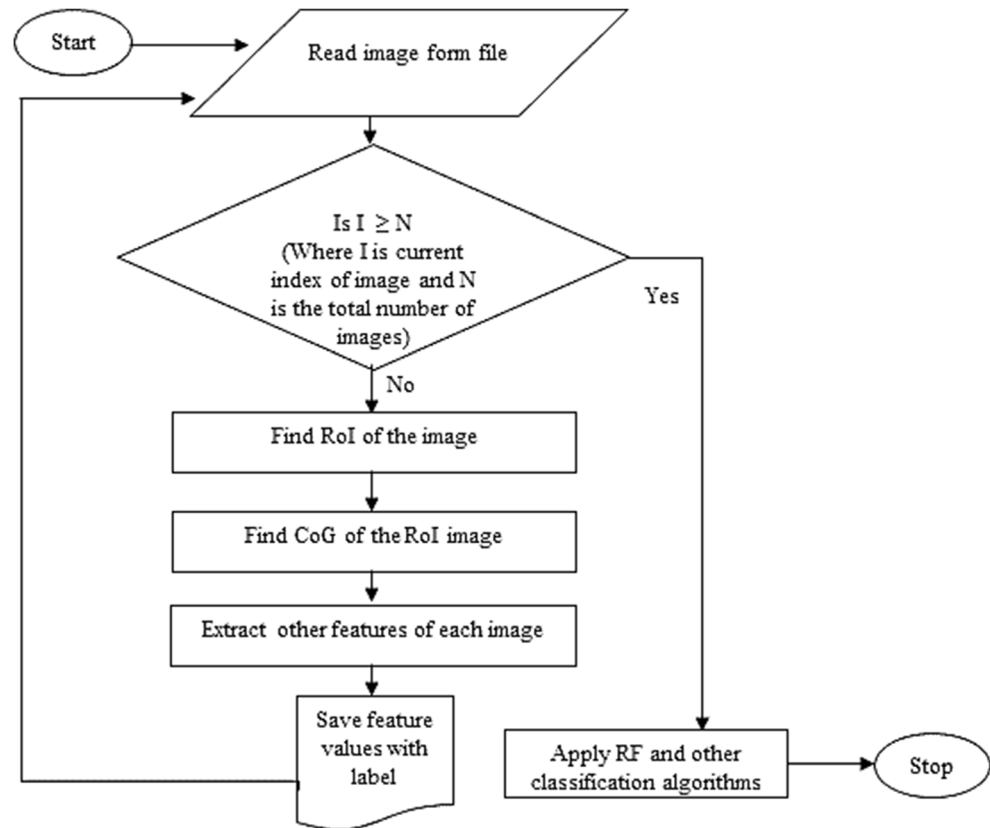
- The region of interest (ROI) detection using Euclidean distance and Manhattan distance metrics is tested by Kar et al. (2019a, b). It is found that the Euclidean distance metric selects the most appropriate region of an image. Here, using the algorithm mentioned in Table 5, the ROI of a resized image (C , size = $m \times n$) is identified.

Rotation-size-translation invariant

The rotation invariant image is used to find CoG. Here the rotation invariant image is generated by rotating the original image $I^{(0)}$ to $I^{(90)}$ and $I^{(180)}$ to $I^{(270)}$. These are the 90, 180, and 270 degree rotated images. These four images are then added together and divided by four to construct an image that is translation and rotation invariant (Onodera et al. 1992). The model is given in Fig. 2.

Table 4 TC and number of images used for dataset creation. Source: RSMC, New Delhi, IMD; Best track data (<http://www.rsmcnwdelhi.imd.gov.in/>)

TC name/basin Intensity scale	Year												Total
	2018	2017	2016	2015	2014	2013	2012	2011	2010	2009	2008	2007	
MEKUNU/ARB	20	NA	NA	20	20	20	20	20	20	20	20	20	100
ESCS	10	10	10	10	10	10	10	10	10	10	10	10	100
VSCS	10	10	10	10	10	10	10	10	10	10	10	10	100
SCS	10	10	10	10	10	10	10	10	10	10	10	10	100
CS	10	10	10	10	10	10	10	10	10	10	10	10	100
DD	10	10	10	10	10	10	10	10	10	10	10	10	100
D	10	10	10	10	10	10	10	10	10	10	10	10	100
Total:	70	50	50	70	70	70	70	70	70	70	70	70	600

Fig. 1 Flowchart of the proposed methodology

Here the rotation invariant image is generated using mean normalized ED (MNED) stated in the “**Feature extraction**” section below. MNED is calculated based on Euclidean distance between CoG and other points of the image. MNED can be used to recognize TC images of different sizes. The Euclidean distances must be normalized.

Feature extraction

Invariant TC recognition is to identify a TC independently of its position and size. Satellite TC images of same class may suffer from size- and position-related problems which cause reduction of accuracy. The central feature of TC towards the rotation-size-translation invariant TC recognition is center of

gravity (CoG). The CoG is a key feature and the subsequent features are derived from the CoG in order to construct a unique feature vector. The TCs of different classes have typical pattern aside from their other physical properties. These patterns are very useful for classification. For example, Fig. 3 a and b are taken from TC Vardha (<https://www.nrlmry.navy.mil/tcdat>, 2016) of VSCS and SCS classes. The patterns of both cyclones are different and the features also differ from each other.

The feature extraction process has been explained in the following (a to j).

- a) Finding the center of gravity (CoG)

Table 5 Algorithm for ROI detection

<i>Input: A TC image (gray scale)</i>
<i>Output: A RoI image (gray scale)</i>
Step1: Find CoG using equation 1 and 2 for C_{mn}
Step2: Calculate Euclidian distance (ed) $c[i,j] \neq 0$ using the equation 3
Step3: Calculate average Euclidean distance d_i
Step4: Check for all pixels present in image if $ed_k > d_i$ then $c[i,j] = 0$ else do nothing
Step5: stop

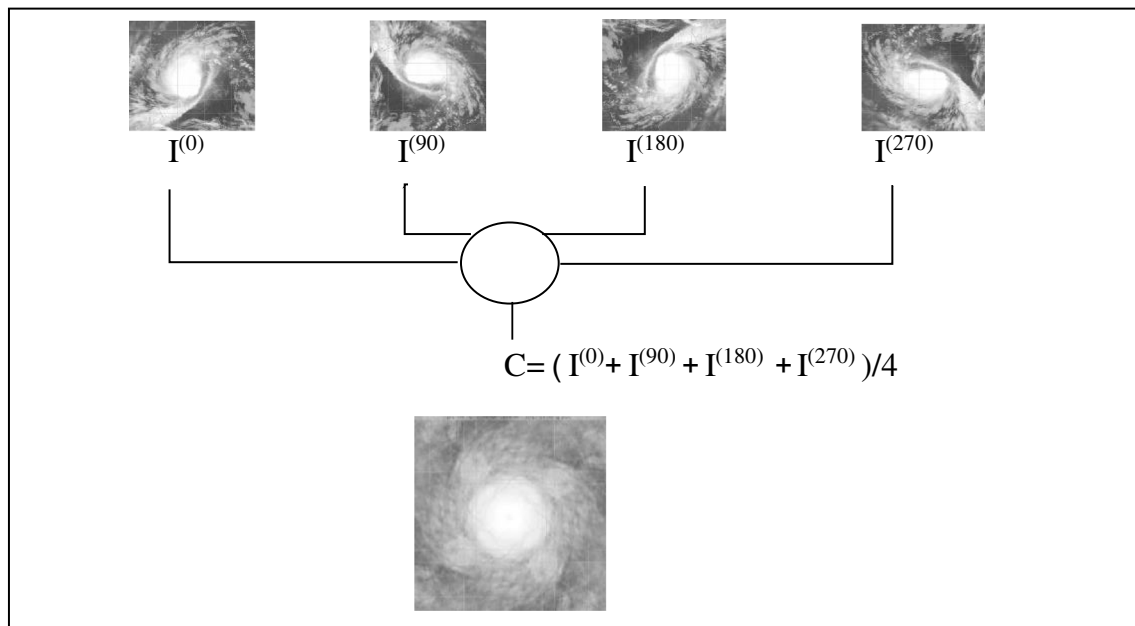


Fig. 2 Rotation-translation invariant model

Equations 1 and 2 are applied to find CoG. Figure 5 shows that the CoG is (3,3). CoG of the original image is shown in Fig. 4b.

b) Euclidean distance (ED)

It is already proved that ED is a rotation invariant distance (Moon et al. 2012). The Euclidean distance of an

$$ed_k = \sqrt{(m - m_{\text{cog}})^2 + (n - n_{\text{cog}})^2} \quad (3)$$

The ED for m th and n th pixel of C is calculated using the above equation (Eq. 3). The ed_k is the ED from the k th nonzero element to the CoG of the m th and n th pixel. An example is TC image $C_{5 \times 5}^1$ (Fig. 5), where 3,3 is CoG and $ed_{\text{max}} = 2.8$.

c) Mean normalized ED (MNED)

$$\text{MNED} = \frac{1}{n} \sum_{k=1}^{i \times j} \frac{ed_k}{ed_{\text{max}}} \quad (4)$$

The MNED is calculated from Eq. 4. The MNED is the mean value of all normalized ED (NED). NED is calculated from ed_k and the maximum Euclidean distance ed_{max} . The ED of the k th nonzero element from the CoG is ed_k , and $\text{max } ed_{\text{max}} = \text{maximum}(ed_k)$. The objective of the NED is to recognize TCs of different sizes in order to achieve a normalized result for comparison. The MNED is calculated using Eq. 4. This MNED is further used to find variance using Eq. 5.

d) Variance (V)

$$V = \frac{1}{n-1} \sum_{k=1}^n \left(\frac{ed_k}{ed_{\text{max}}} - \text{MNED} \right)^2 \quad (5)$$

Fig. 3 a TC Vardha, scale: VSCS type. b TC Vardha, scale: SCS

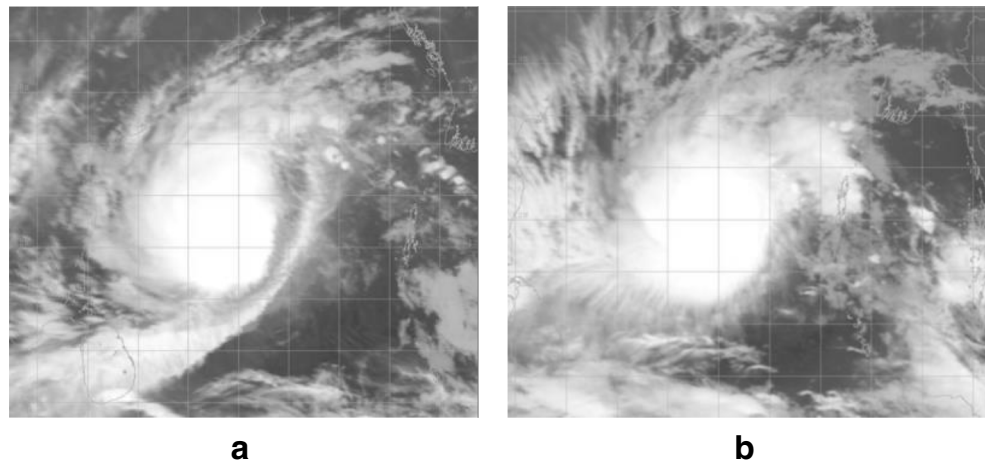
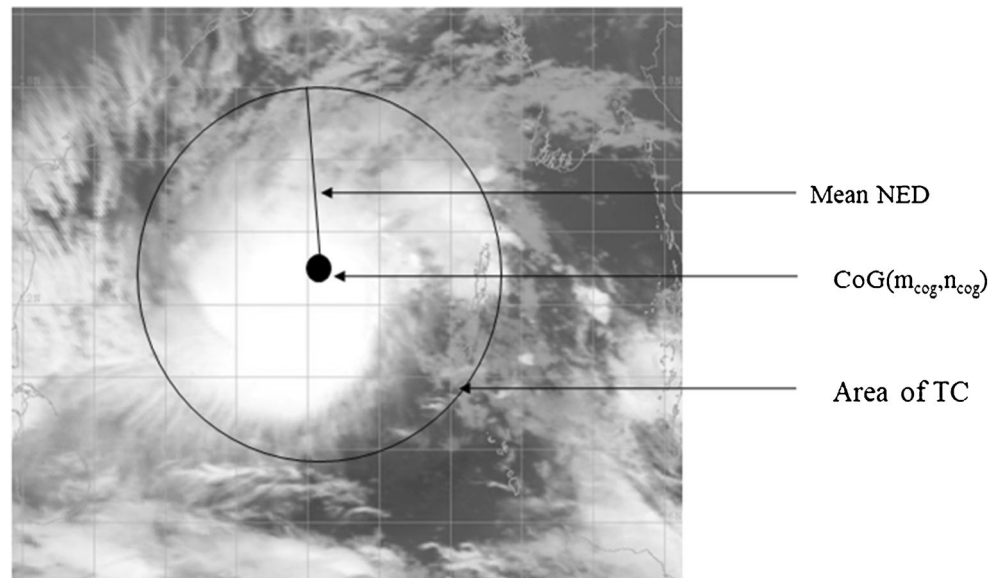


Fig. 5 Area and MNED of a TCe) Density (D)

The density of the image is calculated using sum of the nonzero elements and the area of the circle circumscribing the TC image where $r = ed_{\max}$;

$$D = \frac{1}{(\pi * ed_{\max})^2} \times \left(\sum_{m=1}^i \sum_{n=1}^j c_{mn} \right) \quad (6)$$

f) Decentrality (DC)

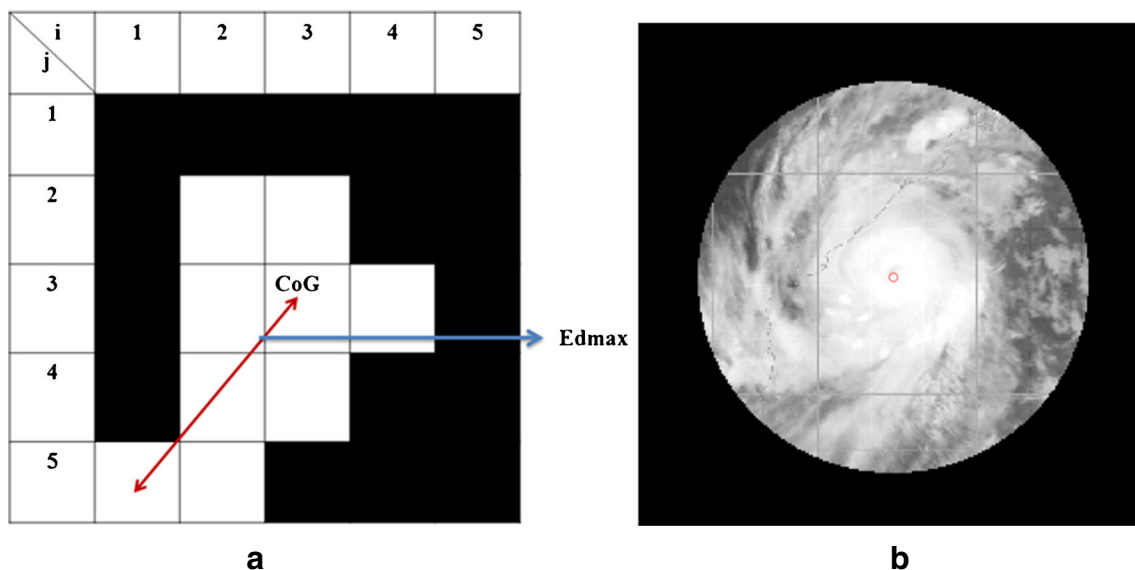
$$DC = \frac{ed_{\min}}{ed_{\max}} \quad (7)$$

where ed_{\min} = minimum (ed_k) for $k = 1$ to $i \times j$.

g) Area of a TC (A)

Based on the MNED, an approximate circular area is calculated to define the area of TC.

$$A = \pi \times MNED^2 \quad (8)$$

h) The zero-order moment of TC image in ROI ($M_{0,0}$)**Fig. 4** a CoG of an image $C^I_{5 \times 5}$. b ROI of a TC image and its CoG (red circle)

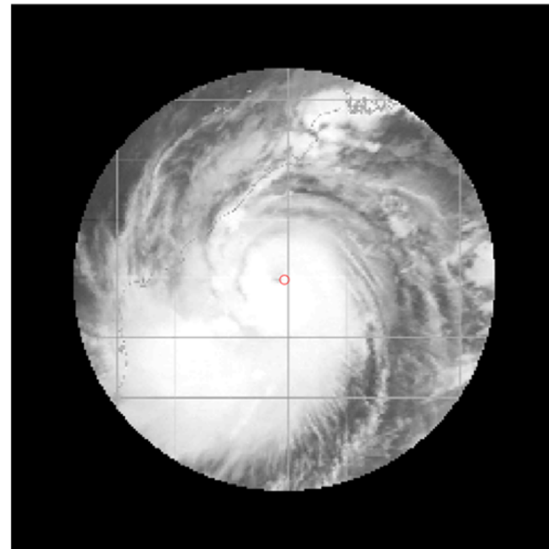
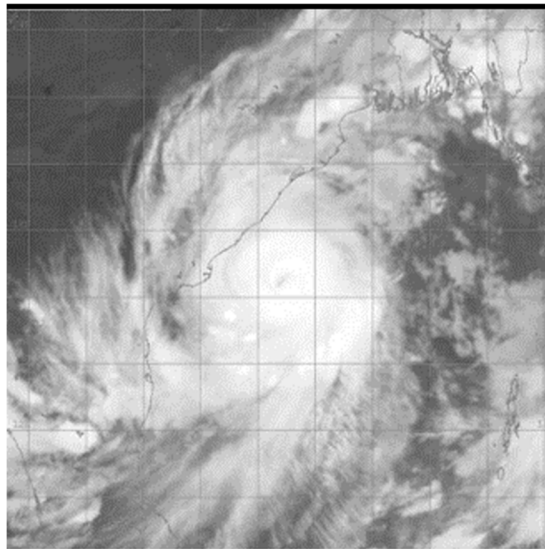


Fig. 6 Gray scale image and corresponding ROI image of a TC

The zero-order moment of an image gives total number of pixels present in the region of interest (ROI) area of a TC. The ROI of a TC image is generated based on the algorithm proposed by Kar et al. (2019b) (Fig. 6). This method is explained below in brief.

The zero-order moment is calculated based on Eq. 9.

$$M_{0,0} = \sum_{i,j \in \text{ROI}} I(i,j) \quad (9)$$

where $I(i,j)$ is the intensity value of an image and it is 1 for binary image.

i) Entropy

This statistical measures is used to find the randomness of a texture feature of an input image. It is defined by the following formula:

Table 6 Feature vector of Fig. 7a

Features	Values
CoG (x,y)	(97px, 101 px)
Mean	39 px
Variance	0.047
Density	0.387
Decentricity	0.012
MNED	81.27 px
Maximum Euclidian distance	7546 px
Area	4758 sqpx
zero-order moment	8051 pxs
Entropy of ROI image	7.361
Entropy of input image	4.289

$$E_{\text{roi}} = \sum_m \sum_n p_{\text{roi}} \ln p_{\text{roi}} \quad (10)$$

$$E = \sum_m \sum_n p_i \ln p_i \quad (11)$$

where p_{roi} and p_i are the normalized histogram counts of the ROI image and original image respectively. When entropy is calculated, the zero intensity values are ignored.

Classifiers

The second step is a classification problem with the six different classes of cyclone evolution.

Naïve Bayes

Naïve Bayes (NB) is use to classify an object. This is a probabilistic classifier based on Bayes' theorem. The representation of a vector with m number of features is given below:

$$x = (x_1, x_2, \dots, x_m) \quad (12)$$

The Bayes theorem for calculating posterior probability is:

$$P(a|x) = \frac{P(x|a)P(a)}{P(x)} \quad (13)$$

where $P(a|x)$ is the posterior probability, $P(a)$ is the prior probability, $P(x)$ is the prior probability, and $P(x|a)$ is the probability of predictor class.

Support Vector Machine

Support Vector Machine (SVM) depends on statistical learning theory and is proposed for solving pattern matching

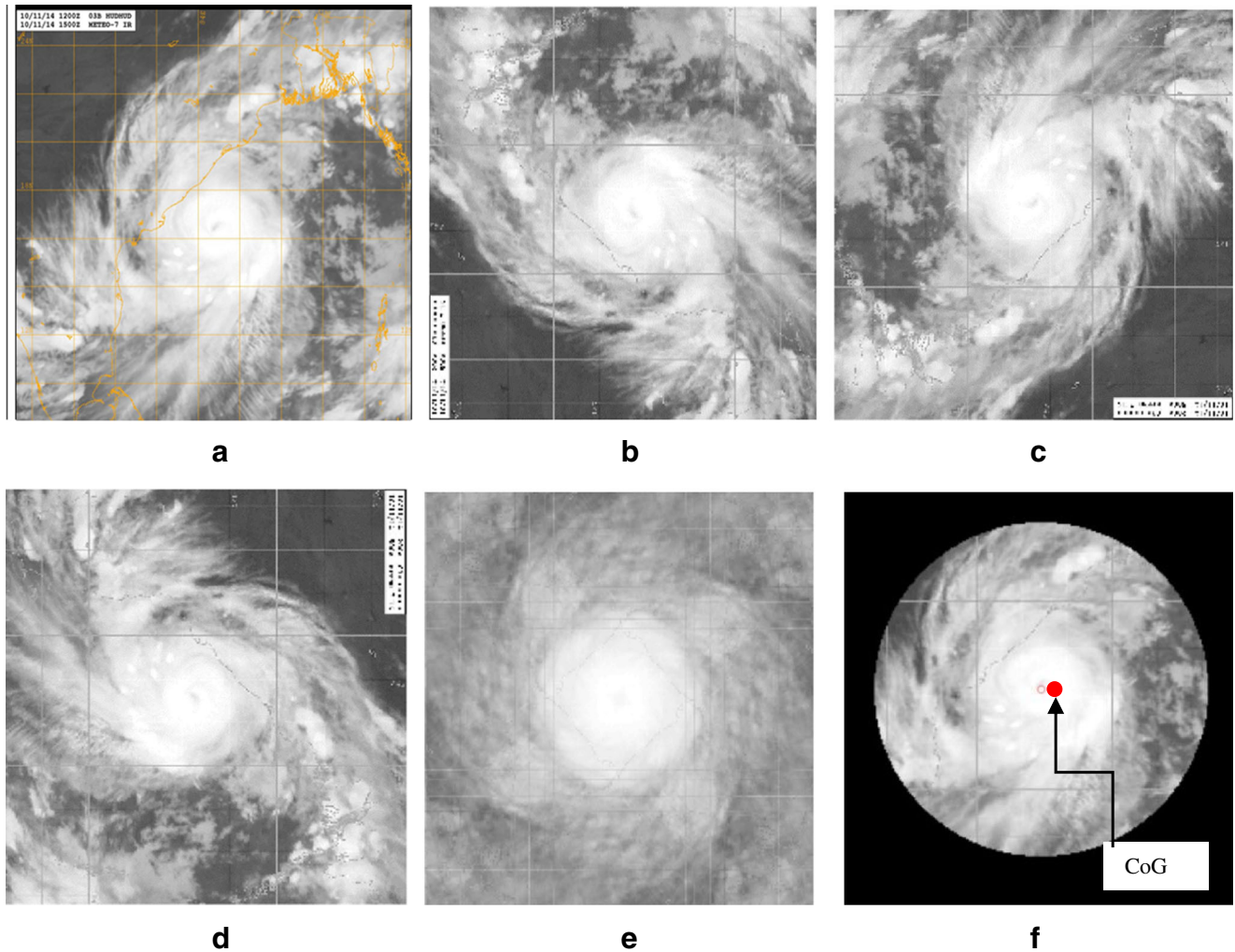


Fig. 7 **a** ESCS image of HUDHUD dated 10th November 2014 (I). **b** Gray image with 90° rotation (I^{90}). **c** Gray image with 180° rotation (I^{180}). **d** Gray image with 270° rotation (I^{270}). **e** Summed image (C). **f** ROI image with CoG

problems (Cortes and Vapnik 1995). Initially, SVMs were intended for binary classification. SVM uses a hyperplane which maintains highest margin between two classes. This margin is derived from the sum of the distances to the hyperplane from the closest points of the two classes (Cortes and Vapnik 1995; Vapnik 1998).

The equation of hyperplane for every class c and points x has the following constraints:

$$w \cdot x_i + b \geq 1, \text{ if } c_i = 1 \quad (14)$$

$$w \cdot x_i + b \leq -1, \text{ if } c_i = -1 \quad (15)$$

where b is the constant and w is the weight vector. The linearly separable data may lead a distinctive global minimum value.

Random Tree

Random Tree (RT) works like decision tree. Random Tree selects a set of attributes randomly. This subset of attributes

is used for classification. The reason behind choosing RT over decision tree is this model performs better than decision tree.

Logistic Model Tree

The Logistic Model Tree (LMT) is a combination of Logistic Regression and Decision Tree model (Landwehr et al. 2005). This model can be used for multi-class target variables. The logistic regression function associated with each leaf node finds the class probability. $l_t(x)$ is the logistic regression function for t th terminal node. S_t represents a region with a leaf node. The model is represented by the below equation.

$$l(x) = \sum_{t=1}^T l_t(x) I(x \in S_t) \quad (16)$$

$$I(x \in S_t) = 1 \quad \text{if } x \in S_t$$

$$= 0 \text{ otherwise}$$

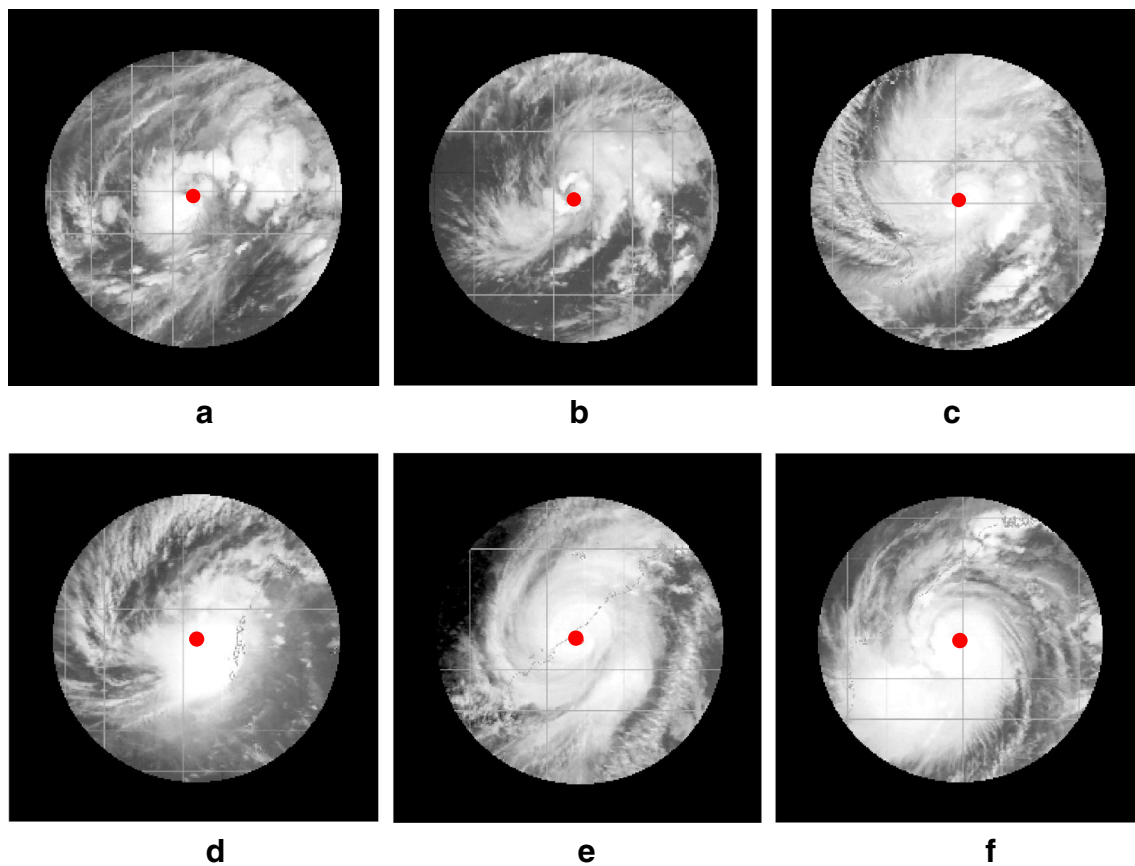


Fig. 8 **a** CoG of D type image. **b** CoG of DD type image. **c** CoG of CS type image. **d** CoG of SCS type image. **e** CoG of VSCS type image. **f** CoG of ESCS type image

Random Forest

The Random Forest (RF) classifier is an ensemble of decision trees and is an example of tree-based supervised machine learning algorithms used for classification tasks. RF is capable of developing a strong learner from a group of individual weak learners. The proposed work is tested using decision tree and RF algorithms and it yields better results in RF. It uses several decision trees and each tree contributes a decision based on votes. The class with majority of vote is selected

by the forest for the vector (Breiman 1999; Pal 2005). The selection of class for a feature vector is done by following idea:

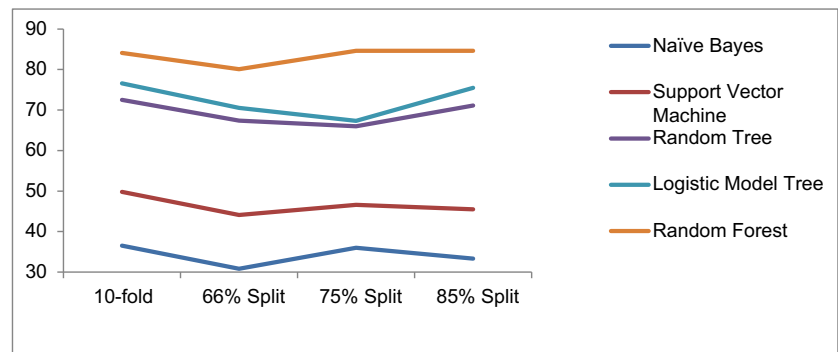
$$RF_c = \text{majority_vote}\{CP(x)\}_{c=1}^N \quad (17)$$

where $C \in N$, and $CP(x)$ is the class prediction of a feature vector x . Total number of classes is N .

The Gini Index (GI) used by RF towards best split selection. This index also measures the impurity of a node with respect to the rest of the classes.

Table 7 Correctly classified instances (in %)

Name of method	Test option			
	10-fold cross-validation	66% split	75% split	85% split
Naïve Bayes	36.5	30.8	36	33.3
Support Vector Machine	49.8	44.1	46.6	45.5
Random Tree	72.5	67.4	66	71.1
Logistic Model Tree	76.6	70.5	67.3	75.5
Random Forest	84.1	80.1	84.6	84.6

Fig. 9 Performance analysis of various classifiers

In a training set R , to select one instance at random and assuming that it belongs to a class C_i , the GI can be written as:

$GI = \sum_{j \neq i} (f(C_j, R)/|R|) (f(C_i, R)/|R|)$ (18) where $f(C_i, R)/|T|$ is the probability of the selected case which belongs to class C_i .

Results

Construction of feature vector

Features of 600 images (mentioned in Table 3) of various classes are extracted based on Table 6. These extracted features of each image are stored in a file with class labels (D, DD, CS, SCS, VSCS, ESCS). The entire work was carried out on Octave 4.2.0 (Eaton et al. 2016). The ROIs of the images are extracted based on the algorithm explained in Table 5. An example of the ROI image with CoG of the original image is shown in Fig. 7. The rotation invariant image and CoG of the ROI are given in Fig. 7.

Table 8 Attribute selection on all input data

Feature name	Feature number	Rank	Rank score	Feature importance based on average impurity decrease
CoG Xval	a0	1	0.1975	0.61
V	a4	2	0.1643	0.58
DC	a6	3	0.1634	0.57
Max ED	a2	4	0.1634	0.56
M_0	a9	5	0.1408	0.55
D	a5	6	0.1244	0.53
M	a7	7	0.1236	0.51
CoG yval	a1	8	0.1188	0.5
A	a3	9	0.1073	0.5
E_{ROI}	a10	10	0.0619	0.5
E_{input}	a11	11	0.0499	0.47
Min ED	a8	12	0.0000	0.0

The CoG of rotation-translation invariant image is shown in Fig. 7f. It has been observed that the CoG of CS, VCS, VSCS, and ESCS images coincides with the eye.

CoG of some TC images is shown in Fig. 8a–f. CoG of most of the TC images coincides with the dense cloud or eye of the TC.

Table 6 shows the feature value associated with above image I.

P_x pixel

Similarly, the feature vector of 600 images with class label is stored for classification purpose.

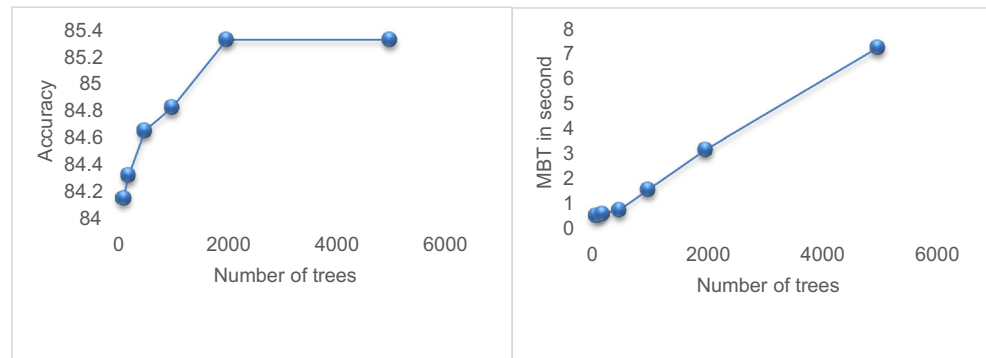
Modeling performance

The extracted features of 600 images are further used for the performance analysis using the Weka data mining tool (Frank et al. 2016). Naïve Bayes (NB), Support Vector Machine (SVM), Random Tree (RT), Logistic Model Tree (LMT), and Random Forest (RF) classifiers are used to check the performance. Here, the correctly classified instances of the abovementioned classifiers in 10-fold cross-validation with 66%, 75%, and 85% splits are shown in Table 7.

The accuracy of the RF classifier is better than of the other classifiers. The major advantage of the RF classifier is its usefulness towards multiclass classification. RF is an ensemble model classifier which is applied on a group of individual weak learners to form a strong learner together to achieve highest accuracy. The RF classifier forms many decision trees and the final outcome is evaluated depending on voting of these trees. Furthermore, it works better when there is a large number of training data points, whereas the use of SVM causes overfitting. All predictors are separated into various classes by finding the maximum margin.

NB assumes that the features are independent. Naïve Bayes is a linear classifier. It predicts class of an input based on probability value and makes the prediction using a threshold. But, due to the linearity, NB cannot work well for nonlinear classification problems. Also, in the absence of a class label with a particular feature, the frequency-based probability is automatically set to zero, which causes erroneous probability estimates. LMT is a decision tree (DT) with leaves that

Fig. 10 a, b Correctly classified instances and model build time (MBT) with respect to number of decision trees



provide piecewise linear regression, while DT uses constants for its leaves. It is good for training data but not for test data and results in overfitting. The cross-validation method is used in Logistic Model Tree to find a number of iterations to prevent overfitting of training data. The logistic regression model is based on the LogitBoost algorithm to find least-squares fits for each class. LMT is found to work well on training data but not on validation data and there is also overfitting.

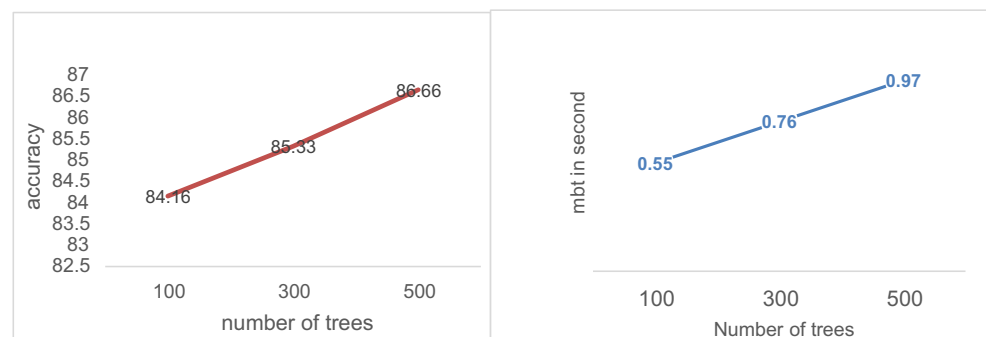
The Random Tree uses a random subset of training pixels and reduces overfitting. Due to the random nature of attribute selection, the accuracy of this classifier is better than of classical decision tree but results for RF are better as the latter uses multiple DT. These are the main reasons for selecting RF over NB and SVM, RT, and LMT. The results of these five classifiers are shown in Table 7. It is also observed that the accuracy of LMT is more than of NB, SVM, and RT but less than of RF. The RF classifier works with multiple decision trees and voting mechanism on decisions received from these decision trees.

Figure 9 shows that the performance of Random Forest outperforms other machine learning algorithms.

Feature subset selection

The size of the feature vector is further reduced to achieve better result using the attribute ranking technique (Table 8). The Symmetrical Uncertainty Ranking Filter is used during selection process. The rank of each feature is evaluated based on all training data.

Fig. 11 a, b Correctly classified instances and model build time (MBT) with respect to number of decision trees in 85% split



We have used a standard feature importance finding technique which is available in Weka (Frank et al. 2016). It is based on the average impurity decrease of a node. The probability of each node can be calculated from the number of samples used by that node, divided by the total number of samples. The significance of higher value is that the higher the value the more important the feature.

If $S = \{a_0, a_1, \dots, a_{11}\}$ is the set of all features and S_1 is a subset of S ; then, $S_1 = \{S - a_8\}$. The $|S| = 12$ and $|S_1| = 11$. The accuracy of the RF classifier is a little higher if we select S_1 . The accuracy is increased by 0.4 (approximately) in the 10-fold cross-validation test mode.

In the “[Parameter tuning and performance estimation of the Random Forest algorithm](#)” section, it is shown that the accuracy of 10-fold cross-validation on the S_1 feature set is 85.33. The result of 85% test split (85% data for training and 15% data for testing) is 86.66.

Parameter tuning and performance estimation of the Random Forest algorithm

The performance of the RF algorithm is better than of other algorithms with 100 trees considered. The maximum depth is 10. Furthermore, the RF algorithm is tuned and tested in 10-fold cross-validation test mode. It is observed that the performance of RF is further increased from 84.4 to 85.33% with 2000 decision trees. Figure 10 a shows that the accuracy of the RF algorithm increases until 2000. The accuracy of the system acquires a plateau after 2000. Figure 10 b shows that the

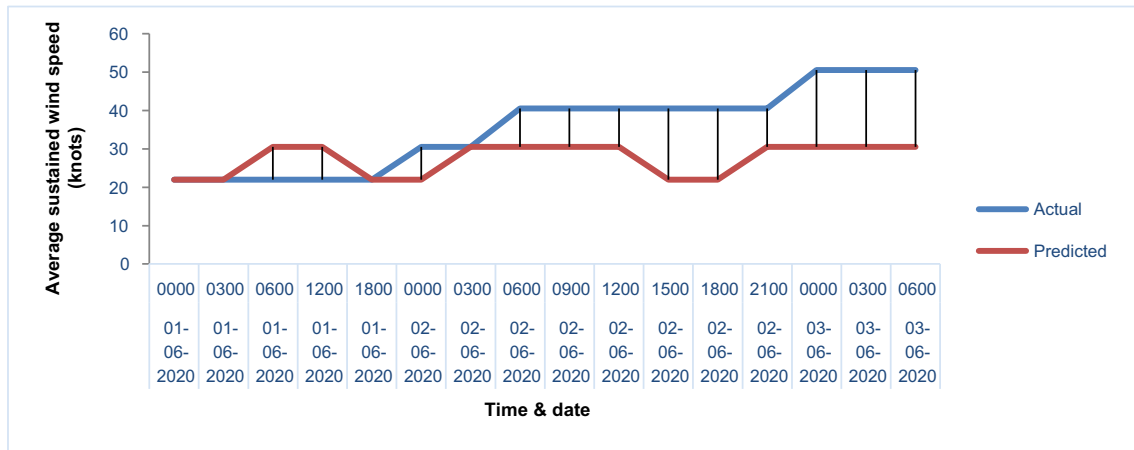


Fig. 12 Time-series comparison of the validation results of 85% split model with IMD best track data of cyclone NISARGA during June 1–3, 2020

minimum build time for the RF model is proportional to the number of trees.

Similarly, the correctly classified instances for 85% split with 100, 300, and 500 trees are shown in Fig. 11a. Model build time with 85% test split and 100, 300, and 500 trees is shown in Fig. 11b.

In addition, we tested our models with the latest cyclones NISARGA (01st June 2000, 0000 UTC to 3rd June 2020, 6000 UTC) and AMPHAN (16th May 2020, 0000 UTC to 17th May 2100 UTC) in order to calculate the general estimation performance of our models (Figs. 12 and 13). The proposed model is used for RMSE prediction of NISARGA (12.5 knots) and AMPHAN (16.5 knots). Results show that the proposed model successfully learned from the TC image dataset.

Discussion

This work is compared with some of the previous works which are based on feature extraction techniques. The feature

vector analysis (Kar and Banerjee 2018), MLP (Kar et al. 2019a), and RF classifier are applied on geometric features of a TC. The RF classifier performs best as shown in Fig. 14 for the intensity classification task using TC images based on the proposed feature extraction technique.

Table 9 represents the accuracy and kappa coefficient of RF over the other classifiers. RF is an ensemble model classifier which is applied to a group of individual weak learners to form a strong learner giving much better results compared to others.

Sensitivity (S) or recall, precision (P), and F -measure (F_M) are calculated using the following equations:

$$S = \frac{TrP}{TrP + FaN} \quad (19)$$

$$P = \frac{TrP}{TrP + FaP} \quad (20)$$

$$F_M = 2 \times \frac{S \times P}{S + P} \quad (21)$$

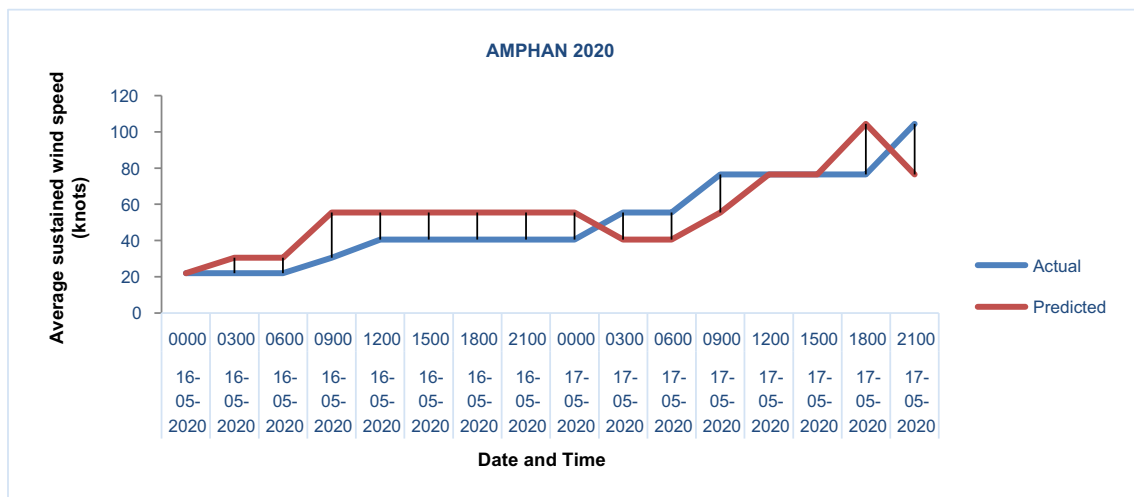


Fig. 13 Time-series comparison of the validation results of 85% split model with IMD best track data of cyclone AMPHAN during May 16–17, 2020

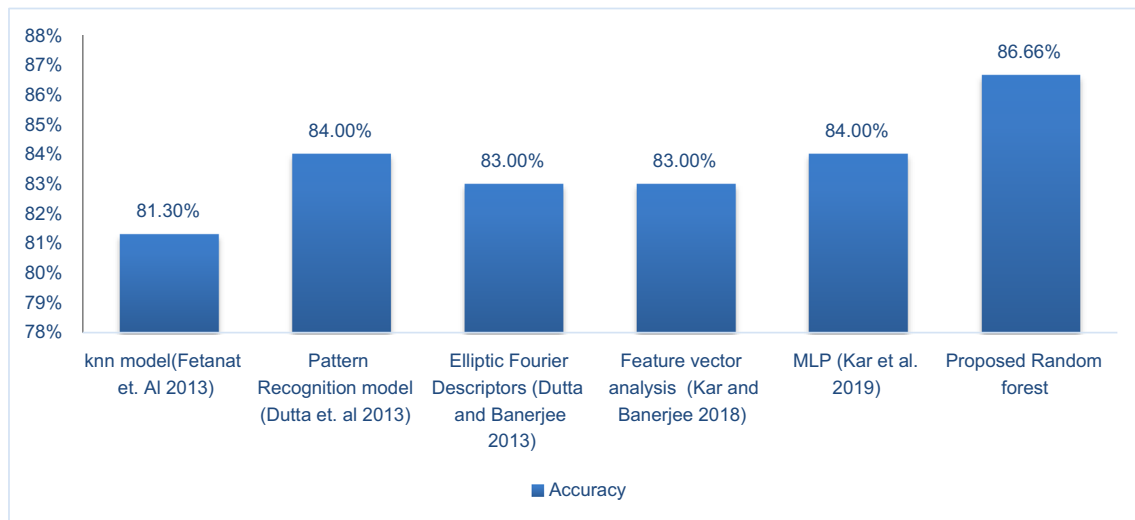


Fig. 14 Accuracy of various feature-based TC intensity estimation methods

Here, TrP is true positive, FaN false negative, and FaP false positive.

Detailed results of all classifiers are shown (10-fold cross-validation test mode) in Table 10.

The performance of a model can be evaluated using root mean square error (RMSE). 9.84 knots is the RMSE of the proposed work and it is calculated based on the following formula:

$$R_{RF} = \sqrt{\frac{1}{600} \sum_{i=1}^{600} (C_n - I_n)^2} \quad (22)$$

I_n is the average sustained wind speed of the n th image predicted by our model. n is the number of images used in each class (i.e., 100). R_{RF} is the RMSE of all images. C_n is the actual average sustained wind speed of each image. Here, $C_n \in C_x$ and C_x represent the average sustained wind speed of each

class $\{D, DD, CS, SCS, VSCS, ESCS\} \in x$. The C_x of each class is calculated using Eq. 23.

$$C_x = \frac{h_x - l_x}{2} \quad (23)$$

where h_x is the higher limit and l_x is the lower limit of class x in TC intensity scale presented in Table 3. For example, sustained wind speed for ESCS is 90 to 119 knots. Here, $l_{ESCS} = 90$, $h_{ESCS} = 119$ and $C_{ESCS} = 104.5$.

C_x of each class is calculated based on Table 11.

The RMSE of 600 images are calculated using the above table. R_{RF} of our model is 9.84 knots. This was calculated based on Eq. 19. I_n is the average sustained wind speed of the n th image predicted by our model and C_n is the actual intensity of that image. If $I_n = 30.5$ and $C_n = 40.5$, then the RMSE of that image is 10.

As discussed, the average RMSE of 600 images is shown in the table. RMSE of our model is 9.84 knots, which is better

Table 9 Kappa coefficient (in %)

Name of method	Test option			
	10-fold cross-validation	66% split	75% split	85% split
Naïve Bayes	0.23	0.15	0.21	0.17
Support Vector Machine	0.39	0.33	0.36	0.35
Random Tree	0.67	0.61	0.59	0.65
Logistic Model Tree	0.72	0.64	0.60	0.70
Random Forest	0.81	0.75	0.81	0.81

Table 10 Sensitivity or recall, precision, and F -measure

Name of method	Test option: 10-fold cross-validation		
	Precision	Sensitivity	F -measure
Naïve Bayes	0.45	0.36	0.32
Support Vector Machine	0.54	0.49	0.47
Random Tree	0.73	0.73	0.73
Logistic Model Tree	0.75	0.75	0.75
Random Forest	0.84	0.84	0.84

Table 11 Average sustained wind speed

Intensity scale	Sustained winds speed (knots)		Average sustained wind speed (knots)
	l_x	h_x	
Extremely severe cyclonic storm (ESCS)	90	119	104.5
Very severe cyclonic storm (VSCS)	64	89	76.5
Severe cyclonic storm (SCS)	48	63	55.5
Cyclonic storm (CS)	34	47	40.5
Deep depression (DD)	28	33	30.5
Depression (D)	17	27	22

than many previous models shown in Table 12. KNN-based feature selection model was used by Bankert and Tag (2002) and Fetanat et al. (2013). Linear regression of the IR features is used by Kossin et al. (2007) with an RMSE of 13.2 knots. The deviation angle variance (DAV)-based technique is used by Pineros et al. (2008), Ritchie et al. (2012) and Ritchie et al. (2014). The RMSE of all of the CNN stated here using IR images are higher than our model. In CNN, the features cannot be gauged individually as the whole image is fed into the convolution layer for feature extraction. The contribution of a given feature towards intensity estimation is thus very difficult to evaluate due to this abstraction.

The RMSE of previous works are shown in Table 12.

Conclusion

Image processing-based TC intensity estimation methods are challenging using the data-driven approaches. There is lack of

image processing-based work on intensity detection of TCs over the Bay of Bengal and Arabian Sea to the best of our knowledge. The intensity scale defined by IMD is mostly used for TC intensity detection. The work proposed here is to classify TCs from its satellite images of D, DD, CS, SCS, VSCS, and ESCS type. The proposed feature extraction techniques are applied on 100 images of each type stated above. The CoG of an image is used here to find rotation invariant patterns to generate other features subsequently. Extracted features are used by the Random Forest algorithm in order to provide best classification result with highest accuracy around 86.66%. The classification accuracy of the proposed method with the RF classifier performed best over the other machine learning classifiers stated here. The RMSE of our model is 9.84 knots, which is lower than many previously stated models. Our results using IR images are comparable to recent studies using MSI images, for instance Lee et al. (2020) with a best optimized value of 8.32 knots, Chen et al. (2019) with RMSE of 8.39 knots, and Yu et al. (2019) with RMSE 7.38 knots. In conclusion, it may be remarked that the proposed algorithm is simple and easy to use and yields accurate results. RF as a classifier worked well with a small number of features as discussed above and yielded better results than CNN algorithms using IR images. Our results indicate that the Random Forest classifier, used successfully in other domains (Richardson et al. 2017; Park et al. 2016; Liaw and Wiener 2002; Roy Chowdhury et al. 2019), is also the best performing algorithm for cyclone intensity classification.

We have found few limitations in our study. First, TC images have latitude grids, longitude grids, and coastlines. These limitations are due to the use of IR images. These limitations may have influenced the feature vector of TC images. Second, only ARB and BOB basins are considered for the study. Finally, this paper has considered 600 images of TCs from 2013 to 2018. In the future, more images of TCs will be taken

Table 12 RMSE of the proposed model and existing TC intensity estimation techniques

SL	Techniques	Authors	RMSE (knots)
1	k-nearest-neighbors (KNN)-based feature selection	Bankert and Tag 2002	19.8
2	Linear regression of IR features	Kossin et al. 2007	13.20
3	Deviation angle variance (DAV)-based technique	Pineros et al. 2008	13–15
4	Neural networks-based TC intensity detection	Kulkarni et al. 2010	22.93
5	k-nearest-neighbors algorithm identifying analog TCs	Fetanat et al. 2013	12.70
6	Statistical analysis of DAV technique	Ritchie et al. 2012	12.90
7	Multiple linear regression model	Zhao et al. 2016	12.01
8	CNN based TC intensity estimation	Pradhan et al. 2018	10.18
9	CNN approach for TC intensity estimation	Combinido et al. 2018	13.23
10	Our model		9.84

to increase the size of the dataset. In addition, with the availability of Meteosat-8 MSI images, we hope that in the future better accuracy with lower RMSE values will be obtained.

Acknowledgements National Satellite Meteorological Center, Indian Meteorological Department for Archive Bulletins 2013–2018. Marine Meteorology Division of United State Naval Research Laboratory (<http://www.nrlmry.navy.mil>) for TC images as mentioned in Table 4.

Declarations

Conflict of interest The authors declare that they have no competing interests.

References

- Archive Bulletins (2013–2018) Indian Meteorological Department, Archive Bulletins DEMS-RSMC Tropical Cyclones, <http://www.rsmcnwdelhi.imd.gov.in/index.php>, Accessed 22 February 2021
- Arora SK, Jha B (2016) Frequently Asked Questions [online]. Indian Meteorological Department. <http://www.imdsikkim.gov.in/wxfaq.pdf>. Accessed 24 February 2021
- Bankert RL, Tag PM (2002) An automated method to estimate tropical cyclone intensity using SSM/I imagery. *J Appl Meteorol* 45:461–472
- Barnes D, Manic M (2010) STRICR-FB, A novel size-translation-rotation-invariant character recognition method. In: *Proceedings of the 3rd International Conf. on Human System Interaction*. Rzeszow: 63–168. <https://doi.org/10.1109/HSI.2010.5514573>
- Breiman L (1999) Random forests - random features. Technical Report 567, Statistics Department, University of California, Berkeley, <https://statistics.berkeley.edu/tech-reports/567>
- Cardone VJ, Cox AT (2009) Tropical cyclone wind field forcing for surge models: critical issues and sensitivities. *Nat Hazards* 51:29–47
- Chen Z, Yu X, Chen G, Zhou J (2018) Cyclone intensity estimation using multispectral imagery from the FY-4 satellite. In: *Proceedings of the 2018 International Conference on Audio, Language and Image Processing (ICALIP)*, pp 46–51. <https://doi.org/10.1109/ICALIP.2018.8455603>
- Chen G, Chen Z, Zhou F, Yu X, Zhang H, Zhu L (2019) A semisupervised deep learning framework for tropical cyclone intensity estimation. In: *Proceedings of the 2019 10th International Workshop on the Analysis of Multitemporal Remote Sensing Images (MultiTemp)*. <https://doi.org/10.1109/Multi-Temp.2019.8866970>
- Combinido JS, Mendoza JR, Aborot JA (2018) Convolutional neural network approach for estimating tropical cyclone intensity using satellite-based infrared images. In: *Proceedings of the 2018 24th ICPR*, pp 1474–1480. <https://doi.org/10.1109/ICPR.2018.8545593>
- Cortes C, Vapnik V (1995) Support-vector networks. *Mach Learn* 20: 273–297
- Dröner J, Korfhage N, Egli S, Mühling M, Thies B, Bendix J, Freisleben B, Seeger B (2018) Fast cloud segmentation using convolutional neural networks. *Remote Sens* 10:1–24
- Dube SK, Rao AD, Sinha PC, Murty TS, Bahulayan N (1997) Storm surge in the Bay of Bengal and Arabian Sea: the problem and its Prediction. *Mausam* 48:283–304
- Dube SK, Jain I, Rao AD, Murty TS (2009) Storm surge modeling for the Bay of Bengal and Arabian Sea. *Nat Hazards* 51:3–27
- Dutta I, Banerjee S (2013) Elliptic Fourier descriptors in the study of cyclone cloud intensity patterns. *International Journal of Image Processing* 7:402–417
- Dvorak VF (1975) Tropical cyclone intensity analysis and forecasting from satellite imagery. *Mon Weather Rev* 103:420–430
- Dvorak VF (1984) Tropical cyclone intensity analysis using satellite data. NOAA Technical Report NESDIS 11:1–47
- Eaton JW, Bateman D, Hauberg SA, Wehbring R (2016) GNU Octave version 4.2.0 manual: a high-level interactive language for numerical computations. <http://www.gnu.org/software/octave/doc/interpreter>. Accessed 22 February 2021
- Fetanat G, Homaifar A, Knapp K (2013) Objective tropical cyclone intensity estimation using analogs of spatial features in satellite data. *Weather Forecast* 28:1446–1459
- Frank WM, Ritchie EA (1999) Effects of environmental flow upon tropical cyclone structure. *Mon Weather Rev* 127:2044–2061
- Frank E, Mark HA, Witten IH (2016) The WEKA workbench online appendix for data mining: practical machine learning tools and techniques. Morgan Kaufmann, San Francisco
- Griffin JS, Burpee RW, Marks FD, Franklin JL (1992) Real time airborne analysis of aircraft data supporting operational hurricane forecasting. *Weather Forecast* 7:480–490
- Jaiswal N, Kishtawal CM (2013) Objective detection of center of tropical cyclone in remotely sensed infrared images. *IEEE J-Stars* 6:1031–1035
- Jin S, Wang S, Li X, Jiao L, Zhang JA, Shen D (2017) A salient region detection and pattern matching-based algorithm for center detection of a partially covered tropical cyclone in a SAR image. *IEEE T Geosci Remote* 55:280–291
- Kar C, Banerjee S (2016) An approach towards automatic intensity detection of tropical cyclone by weight based unique feature vector. In: *Proceedings of the IEEE International Conference on Computational Intelligence and Computing Research (ICCIC)*, pp 1–4. <https://doi.org/10.1109/ICCIC.2016.7919616>
- Kar C, Banerjee S (2018) An image processing approach for intensity detection of tropical cyclone using feature vector analysis. *International Journal of Image and Data Fusion* 9:338–348
- Kar C, Kumar A, Banerjee S (2019a) Tropical cyclone intensity detection by geometric features of cyclone images and multilayer perceptron. *SN Applied Sciences* 1:1099. <https://doi.org/10.1007/s42452-019-1134-8>
- Kar C, Kumar A, Konar D, Banerjee S (2019b) Automatic region of interest detection of tropical cyclone image by center of gravity and distance metrics. In: *Proceedings of the Fifth International Conference on Image Information Processing (ICIIP)*, pp 141–145. <https://doi.org/10.1109/ICIIP47207.2019.8985860>
- Kim M, Park M, Im J, Park J, Lee M (2019) Machine learning approaches for detecting tropical cyclone formation using satellite data. *Remote Sens* 11:1–19
- Kossin JP, Knaff JA, Berger HI, Herndon DC, Cram TA, Velden CS, Murnane RJ, Hawkins JD (2007) Estimating hurricane wind structure in the absence of aircraft reconnaissance. *Weather Forecast* 22:89–101
- Kotal D, Bhattacharya SK (2020) Improvement of wind field forecasts for tropical cyclones over the North Indian Ocean. *Tropical Cyclone Research and Review* 9:53–66
- Kulkarni A, Bankert A, Hadjimichael M (2010) Tropical cyclone intensity estimation using neural networks. In: *Proceedings of the ASPRS Annual Conference*, San Diego, California
- Landwehr N, Hall M, Frank E (2005) Logistic Model Trees. *Mach Learn* 59:161–205
- Lee RST, Lin JNK (2001) An elastic contour matching model for tropical cyclone pattern recognition. *IEEE T Syst Man Cy B*. 31:413–417
- Lee J, Im J, Cha DH, Park H, Sim S (2020) Tropical cyclone intensity estimation using multi-dimensional convolutional neural networks from geostationary satellite data. *Remote Sens* 12:2–24
- Liaw A, Wiener M (2002) Classification and regression by random forest. *R News* 2:18–22
- Liu Y, Racah E, Correa J, Khosrowshahi A, Lavers D, Kunkel K, Wehner M, Collins W (2016) Application of deep convolutional neural

- networks for detecting extreme weather in climate datasets. *Int Conf Big Data*:81–88
- Matsuoka D, Nakano M, Sugiyama D et al (2018) Deep learning approach for detecting tropical cyclones and their precursors in the simulation by a cloud-resolving global nonhydrostatic atmospheric model. *Progress in Earth and Planetary Science* 5:1–16
- Moon YS, Kim SP, Kim J (2012) Fast computation of rotation-invariant distances for image time-series data. In: *Proceedings of the Convergence and Hybrid Information Technology*, vol 7425, pp 516–524
- National Oceanic and Atmospheric Administration (2021) Saffir-Simpson Hurricane Wind Scale <https://www.nhc.noaa.gov/aboutshws.php>, Accessed 22 February 2021
- NOAA (2021) <https://www.ncdc.noaa.gov/data-access/model-data/model-datasets/numerical-weather-prediction>, Accessed 22 February 2021
- Numerical Weather Prediction Division (2021) IMD, <http://nwp.imd.gov.in>, Accessed 22 February 2021
- Observing Systems Capability Analysis and Review Tool (2021) World Meteorological Organization <https://www.wmo-sat.info/oscar/satellites/view/535>, Accessed 22 February 2021
- Olander TL, Velden CS, Turk MA (2002) Development of the advanced objective Dvorak technique (AODT)—Current progress and future directions. *Preprints, 25th Conf. on Hurricanes and Tropical Meteorology*, San Diego, CA
- Olander TL, Velden CS (2007) The advanced Dvorak technique: continued development of an objective scheme to estimate tropical cyclone intensity using geostationary infrared satellite imagery. *Weather Forecast* 22:287–298
- Olander TL, Velden CS (2019) The advanced Dvorak technique (ADT) for estimating tropical cyclone intensity: update and new capabilities. *Weather Forecast* 34:905–922
- Onodera Y, Watanabe H, Taguchi A, Iijima N, Sone M, Mitsui H (1992) Translation and rotation-invariant pattern recognition method using neural network with back-propagation. In: *Proceedings of the Singapore ICCS/ISITA*, 2, pp 548–552
- Pal M (2005) Random forest classifier for remote sensing classification. *Int J Remote Sens* 26:217–222
- Pao TL, Yeh JH (2008) Typhoon locating and reconstruction from the infra-red satellite cloud image. *Journal of Multimedia* 3:45–51
- Park S, Im J, Jang E, Rhee J (2016) Drought assessment and monitoring through blending of multi-sensor indices using machine learning approaches for different climate regions. *Agr Forest Meteorol* 216:157–169
- Piñeros MF, Ritchie EA, Tyo JS (2008) Objective measures of tropical cyclone structure and intensity change from remotely sensed infrared data. *IEEE T Geosci Remote* 46:3574–3579
- Pradhan R, Aygun RS, Maskey M, Ramachandran R, Cecil DJ (2018) Tropical cyclone intensity estimation using a deep convolutional neural network. *IEEE Trans Image Process* 27:692–702
- Pu Z, Kalnay E (2019) Numerical weather prediction basics: models, numerical methods, and data assimilation. In: *Handbook of Hydrometeorological Ensemble Forecasting*. Springer, Berlin, pp 67–97
- Richardson HJ, Hill DJ, Denesiuk DR, Fraser LH (2017) A comparison of geographic datasets and field measurements to model soil carbon using random forests and stepwise regressions (British Columbia, Canada). *GISci Remote Sens* 17:1–19
- Ritchie EA, Valliere-Kelley G, Piñeros MF, Tyo JS (2012) Tropical cyclone intensity estimation in the North Atlantic Basin using an improved deviation angle variance technique. *Weather Forecast* 27:1264–1277
- Ritchie EA, Wood KM, Rodríguez-Herrera OG, Piñeros MF, Tyo JS (2014) Satellite-derived tropical cyclone intensity in the North Pacific Ocean using the deviation-angle variance technique. *Weather Forecast* 29:505–516
- Roy C (2016) An informed system development approach to tropical cyclone track and intensity forecasting. *Dissertation, Linköping Studies in Science and Technology*, Linköping University.
- Roy Chowdhury A, Chatterjee T, Banerjee S (2019) A Random Forest classifier-based approach in the detection of abnormalities in the retina. *Med Biol Eng Comput* 57:193–203
- RSMC New Delhi (2019) Report on cyclonic disturbances over the north Indian ocean during 2018. <http://rsmcnewdelhi.imd.gov.in/images/pdf/publications/annual-rsmc-report/rsmc-2018.pdf>, Accessed 24 February 2021
- Saffir HS (1973) Hurricane wind and storm surge. *The Military Engineer* 423:4–5
- Sakuragi T, Hoshino S, Kitabatake N (2014) Development and verification of a tropical cyclone intensity estimation method reflecting the variety of TRMM/TMI brightness temperature distribution, RSMC Tokyo - Typhoon Center. *Tech Rep* 16:1–15
- Simpson RH (1974) The Hurricane Disaster Potential Scale. *Weatherwise* 27:169–186
- Takahashi HG (2011) Long-term changes in rainfall and tropical cyclone activity over South and Southeast Asia. *Advances in Geosciences* 30:17–22
- TPC-21 Edition (2018) <http://www.rsmcnewdelhi.imd.gov.in/images/pdf/publications/tcp-21/tcp-21-2018.pdf>, Accessed 24 February 2021
- Vapnik V (1998) The support vector method of function estimation. In: Suykens JAK, Vandewalle J (eds) *Nonlinear modeling*. Springer, Boston, pp 55–85
- Velden C et al (2006) The Dvorak tropical cyclone intensity estimation technique: a satellite-based method that has endured for over 30 years. *B Am Meteorol Soc* 87:1195–1210
- Wood VT (1994) A technique for detecting a tropical cyclone centre using a Doppler radar. *J Atmos Ocean Tech* 11:1207–1216
- Yeh KS, Zhang X, Gopalakrishnan S, Aberson S, Rogers R, Marks F, Atlas R (2012) Performance of the experimental HWRF in the 2008 hurricane season. *Nat hazards* 63:1439–1449
- Yip CL, Wong KY, Li PW (2006) Data complexity in tropical cyclone positioning and classification. In: Basu M, Ho TK (eds) *Data complexity in pattern recognition*. Advanced Information and Knowledge Processing. Springer, London, pp 249–270
- Yu X, Chen Z, Chen G, Zhang H, Zhou J (2019) A tensor network for tropical cyclone wind speed estimation. In: *Proceedings of the 2019 IEEE International Geoscience and Remote Sensing Symposium*, 10007–10010
- Yu X, Chen Z, Zhang H, Zheng Y (2020) A novel deep learning framework for tropical cyclone intensity estimation using FY-4 satellite imagery. In *Proceedings of the 2020 the 4th International Conference on Innovation in Artificial Intelligence*, 10–14
- Zhang C, Wang X, Duanmu C (2010) Tropical cyclone cloud image segmentation by the B-Spline histogram with multi-scale transforms. *Acta Meteorol Sin* 24:78–94
- Zhang T, Lin W, Lin Y, Zhang M, Yu H, Cao K, Xue W (2019) Prediction of tropical cyclone genesis from mesoscale convective systems using machine learning. *Weather Forecast* 34:1035–1049
- Zhao Y, Zhao C, Sun R, Wang Z (2016) A multiple linear regression model for tropical cyclone intensity estimation from satellite infrared images. *Atmosphere* 7:1–17